Solar Energy 201 (2020) 398–408

Contents lists available at ScienceDirect

Solar Energy

journal homepage: www.elsevier.com/locate/solener

Synergistics of Cr(III) doping in TiO_2/MWCNTs nanocomposites: Their enhanced physicochemical properties in relation to photovoltaic studies

Ananta G. Dhodamani[a,b], Krantiveer V. More[a], Satish M. Patil[a], Abhijeet R. Shelke[c], Surendra K. Shinde[d], Dae - Youg Kim[d], Sagar D. Delekar[a,*]

[a] Department of Chemistry, Shivaji University, Kolhapur, 416 004 MS, India
[b] Department of Chemistry, Rajarshi Chhatrapati Shahu College, Kolhapur 416 003 MS, India
[c] Department of Physics, Shivaji University, Kolhapur, 416 004 MS, India
[d] Department of Biological and Environmental Science, College of Life Science and Biotechnology, Dongguk University, 32 Dongguk-ro, Biomedical Campus, Ilsandong-gu, Siksa-dong, 10326 Goyang-si, Gyeonggi-do, South Korea

ARTICLE INFO

Keywords:
Cr(III) doping
Optoelectronic studies
Sensitized solar cells
Ternary nanocomposites

ABSTRACT

In the present investigation, optoelectronic modifications of the TiO_2 host lattice through insertion of Cr(III) (0.5–3.0 mol.%) as a dopant and thereafter its composites with MWCNTs prepared using single step *in-situ sol-gel* route and its photovoltaic performance of the hybrids was investigated using Ru(II) based sensitizer. The physicochemical properties (viz. structural, opto-electrical, morphological and charge transfer behavior) of the ternary Cr@TiO_2/MWCNTs NCs are compared with the TiO_2/MWCNTs NC through various spectroscopic (XRD, Raman, UV–Visible DRS, XPS, FT-IR, PL, TRPL and EIS measurements) and microscopic (HR-TEM with SAED) analysis. TRPL and EIS studies reveals that, average life time of the electrons in the excited state increases and interfacial charge transfer resistance decreases after the insertion of Cr(III) ion into the TiO_2 host lattice. After the detailed physicochemical investigations, binder free NCs were deposited on the F:SnO_2 (FTO) by doctor-blade technique using DMF and CH_3CN solvents and then anchored with N719 dye. Finally, sensitized photo-electrode sandwiched with Pt-counter electrode for making the sandwich dye sensitized solar cells (DSSCs) and photovoltaic performance of the assembled devices was measured under AM 1.5 solar simulator for *I-V* and *IPCE* measurements. The $Cr_{.0.010}$@$Ti_{0.990}C$ NCs based DSSCs shows highest photovoltaic conversion efficiency up to η = 7.69% which is 20% (η = 6.18%) higher to that of undoped TiO_2/MWCNTs based DSSCs.

1. Introduction

Recently, semiconducting ternary nanocomposites (NCs) have pivotal role in the leading potential fields of the sustainable survive viz. energy conversion and storage (Chen et al., 2015; Rakhi et al., 2012; Santra and Kamat, 2013), environmental remediation (Deng et al., 2017), catalysis (Miao et al., 2017), sensing (Malik et al., 2018), biomedical (Regulacio et al., 2018), and electronics (Hu et al., 2018) due to their well coverage of the optical region of electromagnetic spectrum (Liu et al., 2013), tuning electronic properties (Mao et al., 2011), and separation of charge carriers (Mondal et al., 2018) etc. Among these potential applications, energy harvesting has a priority choice due the present need of the sustainable energy and available conventional energy sources are insufficient to consume the modern society and also injurious to environment (Yun et al., 2018). Hence, from last two decades investigators intent on the efficient conversion of highly abounded sunlight into electrical energy through low cost, stable dye sensitized solar cells (DSSCs) compared to conventional Si-based solar cells and recently used perovskite based solar cell devices (Mathew et al., 2014). From the discovery of DSSCs (O'regan and Grätzel, 1991), investigators demonstrated, the semiconducting TiO_2 acts as an efficient photocatalyst compared to others such as SnO_2 (Snaith and Ducati, 2010), ZnO (Sakai et al., 2013), Nb_2O_5 (Ou et al., 2012), and $SrTiO_3$ (Tang and Yin, 2015) etc. utilized for the DSSCs. Because of its tunable morphology (Bai et al., 2014), opto-electronic properties (Lee et al., 2012) higher chemical stability (Lee et al., 2012) and higher dye loading capability compared to others (Bai et al., 2014). Also its HOMO-LUMO levels are well matchable to the excited dye (De Angelis et al., 2011), and hence recently reported the highest photovoltaic conversion efficiency up to 14.5% for TiO_2 based DSSCs (Kakiage et al., 2015). With these advantages, it has some constrains viz., it active only in the UV region due to its wider energy band gap (Dette et al., 2014), and

* Corresponding author.
E-mail address: sddelekar7@gmail.com (S.D. Delekar).

https://doi.org/10.1016/j.solener.2020.03.001
Received 10 September 2019; Received in revised form 19 February 2020; Accepted 1 March 2020

hence to resolve these issues various strategies were deployed such as doping (metal/nonmetal), supporting metals, binary NCs through other metal oxides, composites with carbon nanostructures and multi-component hybrid systems (ternary NCs) to tune its optoelectronic behavior and also to overcome its limits (Shwetharani et al., 2019). Among these strategies, investigators emphasis more on the binary and ternary NCs based photoelectrodes for several potential applications due to its extraordinary properties compared to others and host material.

Hence, recently our research group reported the binary TiO_2/carbon nanostructures (TiO_2/RGO and TiO_2/MWCNTs) based NCs for DSSCs through simple, room temperature *in-situ sol-gel* approach and reported the optimized power conversion efficiency up to $\eta = 6.23\%$ for TiO_2/MWCNTs (0.1 wt% of MWCNTs) and $\eta = 5.98\%$ for TiO_2/RGO (0.75 wt % of RGO) NCs respectively (Delekar et al., 2018; Dhodamani et al., 2019). However, these strategies forms the binary composites and also investigators studied it for photovoltaic and reported the comparatively lower power conversion efficiencies to those of recently used perovskite or silicon based solar cells. Hence, to enhance the efficiency of the binary composites further, it is interesting to prepare ternary hybrid composites which will offers new insights to the host semiconductor with remarkable properties which leads to enhance the photovoltaic performance of the NCs. Hence, in literature it is seen that currently only few research groups were studied the optoelectronic properties of the ternary NCs in relation to leading potential areas.

Particularly, Yue et al. designed the ternary Cu/Ni/TiO_2 NCs based electrodes for Li-ion batteries. In which the Ni deposited on the Cu-foil through electro-deposition technique with operating current density of 0.4 A/cm^2 in 10 min. Afterthat, the TiO_2 NPs with binder and some additives spread on the surface of the porous Cu/Ni current collector. Investigator also demonstrated the enhanced electrochemical activity, short Li-ion diffusion pathways, and higher specific surface area of the ternary NCs due to the synergistic effect of porous Cu/Ni with TiO_2 NPs (Yue et al., 2017). Kumar et al. investigated the enhanced photocatalytic degradation of dyes through ternary GO-SnO_2-TiO_2 NCs via. solvothermal route under sunlight irradiation and reported the 96% and 98% degradation efficiency within 60 min and 70 min for methylene blue and Congo red dyes respectively. Also revealed that the enhanced photocatalytic degradation efficiency was attributed to the higher light absorption properties, efficient charge transfer process, higher surface area and superior durability of the ternary NCs (Kumar et al., 2016). Wang et al. fabricated a novel, highly sensitive ternary Au/CuS/TiO_2 NCs based photoelectrochemical biosensor for the detection of glucose, in which TiO_2 nanotubes were prepared by anodization of Ti foils with CuS and Au NPs deposited on it through SILAR chemical route. The fabricated ternary NCs based non-enzymatic photoelectrochemical sensor showed an excellent catalytic activity, favorable selectivity, good reproducibility and higher stability for glucose detection under optimized conditions (Wang et al., 2018). In these investigations authors demonstrated the ternary NCs have excellent physicochemical properties to that of binary and individual host materials and hence recently few investigations studied these ternary NCs based photoelectrodes for photovoltaic studies. Particularly, Pan et al. studied the ternary mercaptopropionic acid (MPA) capped CdS/CdSe quantum dots (QDs) with TiO_2 shown the highest power conversion efficiency up to 5.32%. In which, CdS/CdSe QDs with varying the thickness of CdSe were prepared by high-temperature hot-injection method and capped with MPA as a bi-functional linker and pipetting these MPA-capped CdS/CdSe QDs on the surface of TiO_2 thin film followed by the covering process with ZnS layer and finally sintered at 300 °C (Pan et al., 2012). However, in this investigation, author used very complicated protocols for the fabrication of solar devices and also the reported conversion efficiency was not up to the mark. Also, Yan et al. designed the solid-state DSSCs through co-modified TiO_2 photoanode with fabricated g-C_3N_4 and Ag with hole transporting Material and reported the highest power conversion efficiency up to $\eta = 6.22\%$ (Yan et al., 2016). However, author used costly and sophisticated experimental protocols with different steps required for the preparation of the ternary NCs and hence which causes issues in the connectivity between the different components. Hence, to overcome these limits, it is necessary to design simple, single step, lab-level chemical approach for the preparation of ternary NCs with its proper connectivity, remarkable physicochemical and charge transfer properties in relation to photovoltaic studies.

Hence, in the present investigation, choose Chromium (III) as a suitable dopant for enhancing the optoelectronic behavior of the TiO_2 host lattice of the binary TiO_2/MWCNTs NCs. Because of its resembles properties with Ti(IV) and also the ionic radii of the Cr(III) 0.69 Å is well matchable with the Ti(IV) 0.75 Å ions; it causes the substitution of Ti(IV) ions in the TiO_2 host lattice by Cr(III) and hence it is suitable for making the desired doped TiO_2 with MWCNTs NCs for the fabrication of the ternary NCs (Zhu et al., 2010) and also Xie et al. investigated the effect of the insertion of Cr(III) content (in ppm) into the TiO_2 host lattice through hydrothermal route at 220 °C for 12 hrs. and reported the highest power conversion efficiency up to $\eta = 6.35\%$ for 50 ppm insertion of the doping impurities which appose to an efficiency of $\eta = 5.54\%$ for undoped photoelectrode (Xie et al., 2013). The current investigation also highlights the effect of the insertion of Cr(III) into the TiO_2 host lattice of the TiO_2/MWCNTs with their physicochemical and photovoltaic properties compared to that of the undoped counterparts.

2. Experimental section

2.1. Synthesis of Cr@TiO_2/MWCNTs NCs

Chromium-doped TiO_2/MWCNTs (Cr@TiO_2/MWCNTs) NCs with varying the dopant Cr(III) content in mol.% was synthesized by using *in-situ sol-gel* chemical route at room temperature. Particularly, the stoichiometric amount of Chromium(III) nitrate was dispersed in 10 mL DW separately and directly added into the running synthetic route of TiO_2, before forming the $[Ti(OH)_4]$. Then, whole solution was hydrolyzed by the addition of the NH_4OH, until pH = 10.0 for complete hydroxylation. Afterthat, stoichiometric amount of functionalized-MWCNTs dispersed in 10 mL DW separately with ultrasonic treatment for 10 min and inserted directly into the above mixture (chromium/titanium hydroxide) with continuous stirring. Obtained precipitate washed with DW and finally in ethanol, dried in electric oven and annealed at 450 °C for 2 hrs. The substitution of Ti(IV) ions by Cr(III) ions was varied from 0.0 to 3.0 mol.% and respective ternary Cr@TiO_2/MWCNTs NCs were labeled as $Cr_{0.000}@Ti_{1.000}C$ [(Cr = 0.0 mol.%), (Ti = 100 mol.%)], $Cr_{0.005}@Ti_{0.995}C$ [(Cr = 0.5 mol.%), (Ti = 99.5 mol.%)], $Cr_{0.010}@Ti_{0.990}C$ [(Cr = 1.0 mol.%), (Ti = 99.0 mol.%)], $Cr_{0.030}@Ti_{0.970}C$ [(Cr = 3.0 mol.%), (Ti = 97.0 mol.%)], and C = constant for O_2 and MWCNTs (MWCNTs = 0.1 wt%).

2.2. Device fabrication and testing of DSSCs

Simple doctor-blade technique have been employed for the deposition of binder-free NCs on the surface of F:SnO_2 (FTO) and annealed at 450 °C for two hrs (Delekar et al., 2018). Deposited NCs thin films were sensitized with N719 dye [0.3 mM (1:1 v/v *tert*-butanol and acetonitrile)] for 18 hrs. under dark at room temperature. Then, the dye loaded photoelectrodes were rinsed thrice with the 1:1 v/v *tert*-butanol and acetonitrile solution for removing the unbounded dye. Afterthat, 0.25 cm^2 working area sandwiched with platinum counter electrode [(precursors of Platinum (Platisol, Solaronix) deposited on In:SnO_2 (ITO) by drop casting method and sintered at 450 °C for half hrs.] through 60 μm thick sealing thermoplastic Surlyn sheet at 80 °C. Finally, redox electrolyte (1.0 M LiI + 0.06 M I_2 in propylene carbonate) was injected into the cell through a small hole into the counter electrode, under the vacuum desiccator. Finally, sandwiched devices

measured through photocurrent density voltage curve (*I-V*) and IPCE under one sun illumination using 300 W Xenon lamp solar simulator with AM 1.5G filter.

2.3. Measurements

X-ray powder diffractometer (Bruker D2-Phaser) with Cu Kα radiation (λ = 1.5406 Å) was utilized for the powder X-ray diffraction (XRD) analysis. The Rietveld refinement of the raw XRD data was analyzed through Rietveld FullProf program. The crystal structure models of the desired materials were visualized through VESTA program. Raman measurements were carried out by using the Raman spectrometer (Bruker Multi–RAM). UV–Visible diffused reflectance spectra (UV–Visible DRS) of all the materials were measured through UV–VIS spectrophotometer (LABINDIA, UV 3092). A Fourier transform infrared (FTIR) spectrum was measured with an infrared instrument (Bruker, Tensor 27). JEM-100 CX II transmission electron microscopy was utilized for the analysis of high resolution transmission electron microscopy (HR-TEM) with selected area electron diffraction (SAED) of the samples. Photoluminescence (PL) spectra of the representative samples were recorded by using (JASCO FP-750). Elemental analysis of the samples was measured by using (ESCA VG Multilab 2000, Thermo VG Scientific UK). 300 W Xenon lamp solar simulator with AM 1.5G filter (67005, Newport Oriel Instruments, USA) having source meter (2400, Keithley) under illumination of 100 mW/cm^2 with one sun illumination was utilized for knowing the cell performance of the assembled DSSCs.

3. Results and discussion

Fig. 1 shows the XRD profiles of the synthesized TiO_2 (T), TiO_2/MWCNTs, and Cr@TiO_2/MWCNTs NCs with varying the Cr(III) content (0.5–3.00) in mol.%. The observed peak positions and their reflections 25.37° (1 0 1), 37.86° (0 0 4), 47.98° (2 0 0), 54.01° (1 0 5), 54.98° (2 1 1), 62.53° (2 0 4), 68.90° (1 1 6), 70.24° (2 2 0), 75.08° (2 1 5), 82.74° (3 0 3) are well matches to the anatase phase of TiO_2 (PCPDFWIN # 21-1272). Also, XRD pattern of MWCNTs (Fig. S1, *SI*) shows the characteristics peak positions at 26.35° (0 0 2), 42.81° (1 0 0), 44.96° (1 0 1) matches to the elemental carbon (PCPDFWIN # 41-1487). But, these characteristics peaks are not appeared in the TiO_2/MWCNTs as well as Cr@TiO_2/MWCNTs NCs; it is due to the either least amount of the MWCNTs or shielding of these peaks into the anatase phase of TiO_2

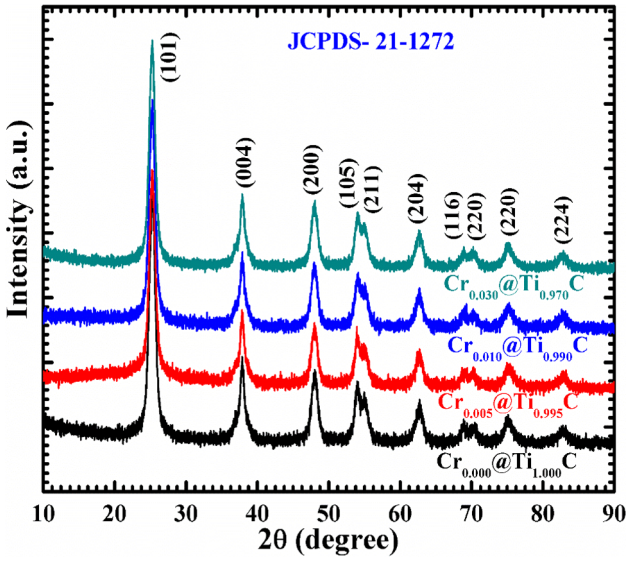

Fig. 1. XRD profiles of TiO_2 (T), TiO_2/MWCNTs, and Cr@TiO_2/MWCNTs NCs with varying the Cr(III) content in 0.5–3.0 mol.%

(Delekar et al., 2018).

The absence of other peaks in the Cr@TiO_2/MWCNTs NCs: indicates the Cr(III) did not forms the chromium oxide and also did not alter the pure anatase phase of TiO_2 in the NCs (Inturi et al., 2014a). However, the insertion of Cr(III) content (0.5–3.0 mol.%) into the TiO_2/MWCNTs NC increases the crystallite size from 8.73 to 7.82 nm (Scherer's formula) and cell volume decreases from 135.54 to 134.11 Å^3 respectively. The various crystallographic cell parameters such as '*a*', '*c*', crystallite size, cell volume and lattice strain are calculated and included in the supporting information (Table S1, *SI*). The slight decreasing the crystallite size and other cell parameters in the NCs after the insertion of Cr content, it mainly due to the ionic radius of the elemental Cr (1.66 pm) slightly lower to that of Ti (1.76 pm); which resides into the TiO_2 host lattice by substitution of Ti(IV) by Cr(III) (Inturi et al., 2014b). It is also seen that, as the content of Cr(III) increases into the TiO_2/MWCNTs NCs, slight change in the peak positions with peak intensity; it again justified through the lattice sites of ions presents into the TiO_2 host lattice of the Cr@TiO_2/MWCNTs NCs.

The quantitative analysis related to structural properties of the XRD data after the insertion of Cr(III) content into the TiO_2/MWCNTs NCs was confirmed by using Rietveld FullProf program. Rietveld refinement patterns of the TiO_2/MWCNTs and Cr@TiO_2/MWCNTs NCs with varying the Cr(III) content is illustrated in the supporting information [Fig. S2, (a to d)]. The final Rietveld refinement results show the goodness fit (χ^2) value around 1.30–1.40 indicates the well extent of fitting. Also, the obtained refinement results show good agreement with the calculated and observed patterns with respect to the various cell parameters applied. The crystallographic cell parameters such as '*a*', '*b*', '*c*' in Å and cell volume 'V' in Å^3 of the TiO_2/MWCNTs and Cr@TiO_2/MWCNTs NCs with varying the content of Cr(III) (0.5–3.0 mol.%) from Rietveld program and calculated from the XRD profiles are presented in Table 1. Other cell parameters viz. Rp and Rwp obtained from the Rietveld analysis are also included in the supporting information (Table S1, *SI*).

All the indexed refinement results of the TiO_2/MWCNTs and Cr@TiO_2/MWCNTs NCs suggest good agreement with the anatase phase of TiO_2. The crystal structure model of the $Cr_{0.010}$@$Ti_{0.990}$C NCs visualized through VESTA after the refinement and displayed in Fig. 2(a) also the position of the elements and their bond length with bond angle are also included in Fig. 3(b). The obtained Ti—O—Ti bond angle with Ti—O bond length from the crystal structure models is included in Table 1. It is seen that, after the insertion of Cr(III) into the TiO_2/MWCNTs NC, the Ti—O—Ti bond angle, and Ti—O bond length enhances, it may be due to the substitution of Ti(IV) by Cr(III) in the Cr@TiO_2/MWCNTs NCs.

Raman spectra of the representative TiO_2/MWCNTs and $Cr_{0.010}$@$Ti_{0.990}$C NCs powders are shown in Fig. 3. It shows the characteristics peaks at ~144.59, ~398.20, ~516.54, and ~640.82 cm^{-1} are well matches to the frequency vibration modes of the anatase TiO_2 (Fig. S3, *SI*) viz. E_g, B_{1g}, A_{1g} and E_g(1) respectively (Tian et al., 2012). Other peaks are not appeared in the frequency region at 100–650 cm^{-1} indicates the prepared NCs free from other phases of TiO_2 viz. rutile and brookite. It also shows the appearance of the D and G bands at 1344 and 1581 cm^{-1} in the NCs along with the vibration bands of anatase TiO_2 corresponding to indicative disorder and ordered graphitic structure of the MWCNTs (Delekar et al., 2018).

Interestingly, after the insertion of Cr(III) content in TiO_2/MWCNTs NC, decreases the most intense peak of the anatase TiO_2 (Eg) with shifting its peaks position into higher Raman shift value (inset of Fig. 3). It was mainly due to the strain gradients originating from interface integration of the Cr(III) content or the particle size distribution in the NCs (Ikeda et al., 2008). Hence, decreasing the peak intensity with shifting its characteristics peak positions in the $Cr_{0.010}$@$Ti_{0.990}$C to that of $Cr_{0.000}$@$Ti_{1.000}$C NC indicates the substitution of Ti(IV) by Cr(III) ions into the TiO_2 host lattice of the TiO_2/MWCNTs NCs (Cao et al., 2013).

Table 1
Crystallographic cell parameters, (Ti—O—Ti) bond angle and (Ti—O) bond length of the Cr@TiO_2/MWCNTs NCs with the varying the content of Cr (III) in mol.%, obtained by using XRD powder analysis and Rietveld FullProf program.

Samples	Cell parameters (XRD)				Cell parameters (Rietveld)					Ti—O—Ti bond angle (degree)	Ti—O bond length (Å)
	a = b (Å)	C (Å)	V (Å^3)	D (nm)	a = b (Å)	c (Å)	V (Å^3)	D (nm)	χ2		
$Cr_{0.000}@Ti_{0.000}C$	3.786	9.454	135.54	8.73	3.786	9.489	136.06	14.56	1.30	169.23	1.9063
$Cr_{0.005}@Ti_{0.995}C$	3.790	9.509	136.66	8.54	3.787	9.487	136.04	14.34	1.36	169.93	1.9190
$Cr_{0.010}@Ti_{0.990}C$	3.787	9.500	136.29	8.43	3.788	9.489	136.09	14.26	1.34	170.01	1.9254
$Cr_{0.030}@Ti_{0.970}C$	3.786	9.354	134.11	7.82	3.786	9.480	136.02	14.11	1.40	169.88	1.9128

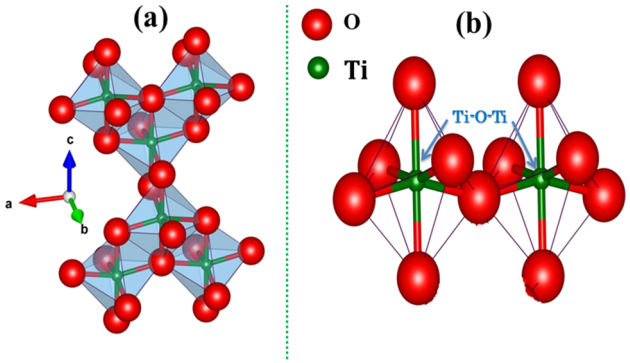

Fig. 2. (a) Crystal structure model of $Cr_{0.010}@Ti_{0.990}C$ NC viewed along with C axis [A large slight blue sphere represents the Ti atoms while a red ball represents the O ions] (b) Ti—O—Ti bonding arrangement in the NC crystal structure, visualized through VESTA. (For interpretation of the references to colour in this figure legend, the reader is referred to the web version of this article.)

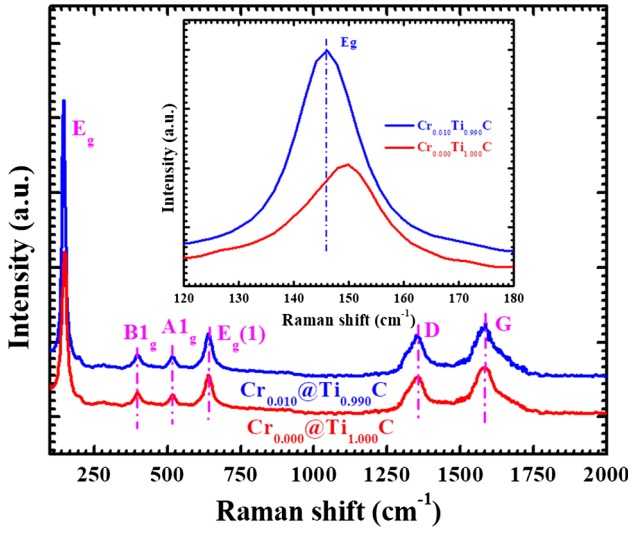

Fig. 3. Raman spectra of representative TiO_2/MWCNTs and $Cr_{0.010}@Ti_{0.990}C$ NCs, shifting of the Eg band after the insertion of Cr(III) in TiO_2/MWCNTs NC (inset).

Fig. 4 (a and b) shows the TEM images of the representative $Cr_{0.010}@Ti_{0.990}C$ NC with resolutions 50 and 20 nm. It is seen that, the well decoration of the Cr@TiO_2 NPs on the surface of MWCNTs having particle size in the range between 6-8 nm. High resolution TEM micrographs of the $Cr_{0.010}@Ti_{0.990}C$ NC shows the well-defined, completely crystalline and highly resolved crystal lattice fringes of the Cr@TiO_2 NPs and the distance from the two respective fringes around 0.351 nm and close to the observed d-spacing value of the sharp peak of the $Cr_{0.010}@Ti_{0.990}C$ NC having reflection (1 0 1).

HR-TEM image also shows the appearance of the MWCNTs with Cr@TiO_2 NPs in the $Cr_{0.010}@Ti_{0.990}C$ NC indicates the well chemical connectivity between the Cr@TiO_2 NPs and MWCNTs (Fig. 4c). The selected area electron diffraction patterns (SAED) of the $Cr_{0.010}@Ti_{0.990}C$ NC shows the usual ring pattern with good intensity indicates the desired NC are good crystalline in nature (Fig. 4d). Also, the observed distance from origin of the ring patterns well matchable to the d-spacing values of the various reflections viz. (1 0 1), (0 0 4), (2 2 0), (2 1 1) calculated from the XRD profile. The well anchoring of the optoelectronically modified Cr@TiO_2 NPs would again enhances the charge collection efficiency of the DSSCs, because the higher conductivity of the MWCNTs tunes the optoelectronic behavior of Cr@TiO_2 NPs (Mao et al., 2018).

To study the optical behavior of the TiO_2 matrix after the insertion of Cr(III) content into the TiO_2 host lattice with incorporation of MWCNTs, the UV–Visible diffused reflectance spectroscopy (DRS) was used in the absorbance mode. UV–Visible DRS spectra of TiO_2 (T) shows the absorption edge in the UV region (385 nm), while it slightly shifted to the visible region (400 nm) with higher absorption intensity after the incorporation of MWCNTs into the TiO_2 [Fig. S4(a), *SI*]. Also, along with the synergistic effect of MWCNTs with TiO_2, the insertion of Cr(III) doping in TiO_2/MWCNTs NC benefits for additional absorption in the red region of the spectrum to that of bare TiO_2 only and TiO_2/MWCNTs NC [Fig. 5(a)]. Because, the insertion of Cr(III), enhances its absorption edge in the region between 400 and 600 nm; it may be due to the 4f states of Cr(III) minimizes the conduction band of TiO_2 and it responsible for absorbing the maximum photon flux of the spectrum (Hwang et al., 2005; Inturi et al., 2014a). Also, as the content of Cr(III) increases in TiO_2/MWCNTs, the short hump observed in the visible region (600–800 nm) with higher absorption intensity in the UV–Visible region (300–600 nm). Confirms, the substitution of Ti(IV) by Cr (III) ions and also it benefits for coverage of the spectrum to that of bare TiO_2 and TiO_2/MWCNTs NC. Overall, the hybrid Cr@TiO_2/MWCNTs ternary NCs based photoelectrode had a potential for absorption of maximum photons in the broad region (UV–Visible) of the spectrum and convert efficiently it into electrical energy (Zhu et al., 2006).

Fig. 5(b) shows the optical energy band gap of the Cr@TiO_2/MWCNTs NCs with varying the content of Cr(III), determined by Tauc plot of the modified Kubelka–Munk function $(\alpha h\nu)^{1/2}$ versus photon energy ($h\nu$) and fixed to the intercept tangent to the x-axis (Delekar et al., 2018). TiO_2/MWCNTs NC decreases the energy band gap from 3.2 to 2.89 eV after the incorporation of MWCNTs [Fig. S4(b), *SI*]. Also, the insertion of Cr(III) content again decreases up to 2.65 eV signifies the insertion of Cr(III) modifies the optoelectronic behavior of the TiO_2 for better separation of charge carriers (Dholam et al., 2009).

The electronic behavior of the semiconducting material after the insertion of Cr(III) into the TiO_2 host lattice of the TiO_2/MWCNTs NCs was studied through Photoluminescence spectroscopy. Fig. 6 shows the PL spectra of TiO_2/MWCNTs and Cr@TiO_2/MWCNTs with varying the content of Cr(III). All the NCs show two distinct emission bands at 412 and 472 nm assigned to the band-band transition and defecate from the oxygen species, having excitation wavelength at 365 nm (Delekar et al., 2018). It is seen that, the insertion of Cr(III) increases in the NCs, the emission peak intensity decreases indicates the better separation of charge carriers and which benefits for enhancing the *Jsc* value of the

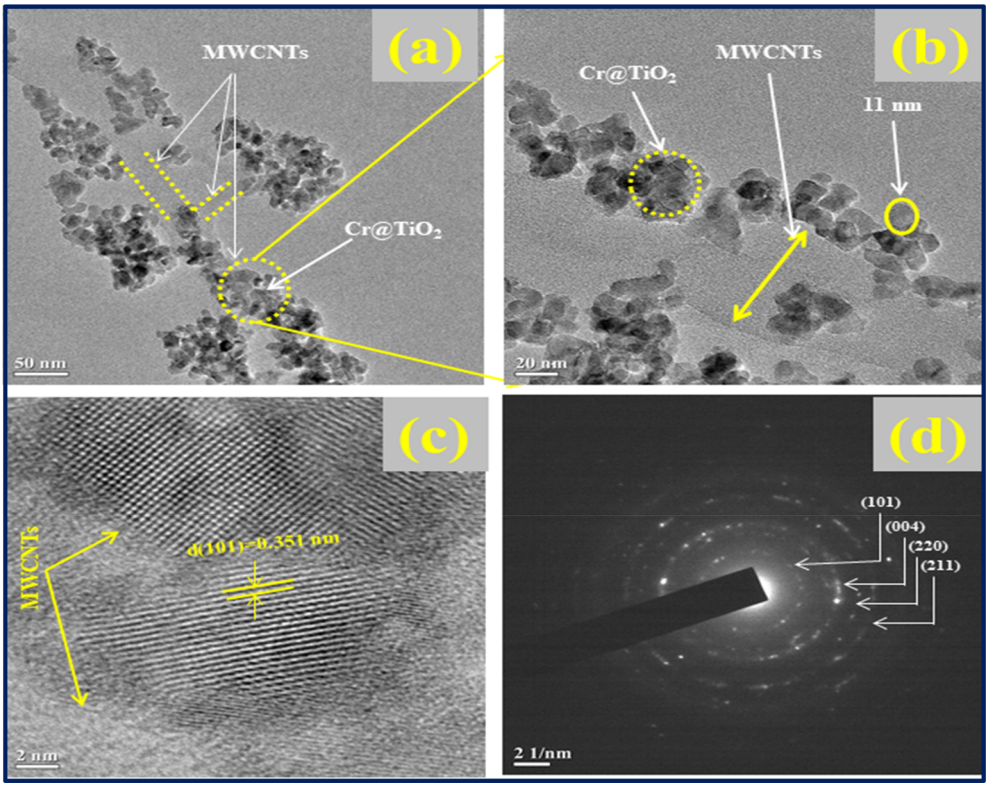

Fig. 4. (a and b) TEM images with resolution 50 and 20 nm, (c) HR-TEM and (d) SAED pattern of $Cr_{0.010}@Ti_{0.990}C$ NC.

DSSCs (Wang et al., 2012).

FT-IR spectroscopy employed to knowing the different functional moieties appeared from the MWCNTs and Cr(III) into the TiO_2; and the results are illustrated in Fig. 7. FT-IR spectrum of TiO_2/MWCNTs shows the frequency regions at 3600–3000, 2810, 2740, 2195, 1601, and 1350 cm^{-1} corresponding to the O—H stretching, C—H stretching, C—OH stretching, C—O stretching, O—H deformation frequency vibrations respectively (Delekar et al., 2018). All these frequency vibrations originated from the functional moieties of the MWCNTs incorporated into the TiO_2. Also, shows the broad frequency vibrations in the range between 900 and 400 cm^{-1} attributed due to the Ti-O, O-Ti-O stretching vibrations from the lattice formation bands of TiO_2 (Shevale et al., 2017).

After the stoichiometric addition of Cr(III) ions into the TiO_2/MWCNTs NCs, it shows all the frequency vibrations of TiO_2/MWCNTs NCs with slight shifting of the peak positions to the higher frequency regions. Also, the Ti-O peak in the range between 900 and 400 cm^{-1} boarder to that of TiO_2/MWCNTs NC, it may be due to the different interfaces of O-Ti-O, Ti-O, Cr-O, Cr-O-Ti, and Ti-O-C after the insertion of Cr(III) content (Mamba et al., 2014). The overall functional investigation of $Cr_{0.010}@Ti_{0.990}C$ NC indicates the substitution of Ti(IV) by Cr(III) ions into the TiO_2 host lattice of the binary TiO_2/MWCNTs NC.

X-ray photoelectron spectroscopy (XPS) is the surface sensitive analytical tool used to confirm the existence and the chemical states of the 'Ti', 'O', 'C', and 'Cr' in the desired Cr@TiO_2/MWCNTs NC. Fig. 8a

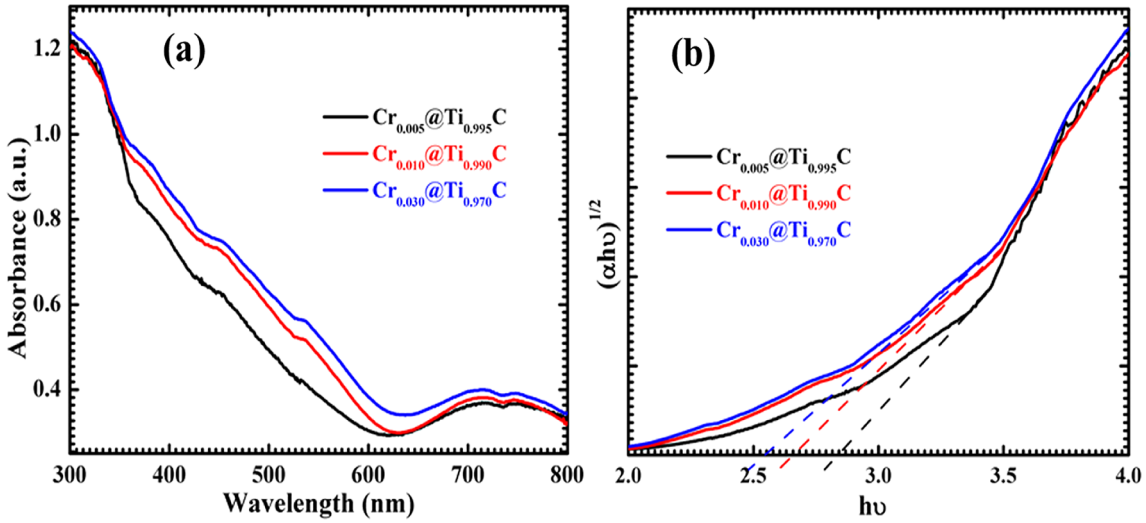

Fig. 5. (a) UV–Visible DRS (absorption mode) (b) Tauc plot $(\alpha h\nu)^{1/2}$ versus photon energy ($h\nu$) of Cr@TiO_2/MWCNTs NCs with varying the Cr(III) content (0.5–3.0 mol.%).

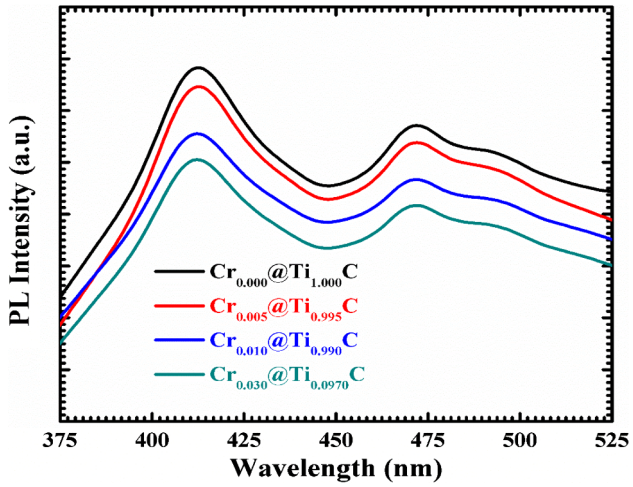

Fig. 6. Photoluminescence emission spectra of TiO_2/MWCNTs and Cr@TiO_2/MWCNTs NCs with varying the Cr(III) content (0.5–3.0 mol.%).

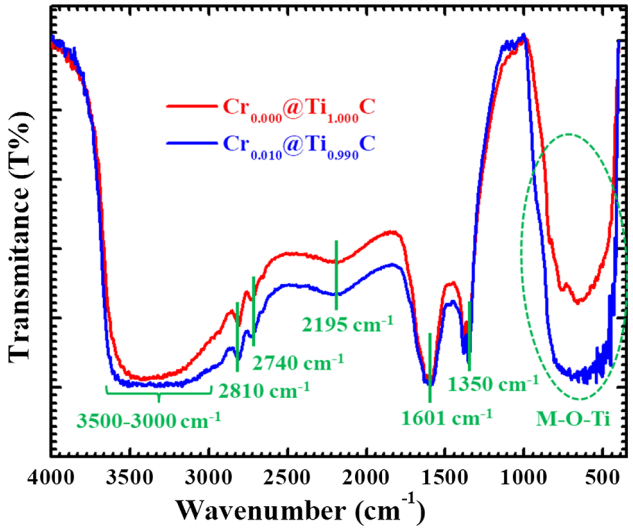

Fig. 7. FT-IR spectra of representative TiO_2/MWCNTs (red line) and $Cr_{0.010}@Ti_{0.990}C$ (blue line) NCs. (For interpretation of the references to colour in this figure legend, the reader is referred to the web version of this article.)

shows the XPS survey spectrum of $Cr_{0.010}@Ti_{0.990}C$ NC, it shows the existence of the 'Ti', 'O', 'C', and 'Cr' in the NC indicates the insertion of Cr(III) with incorporation of MWCNTs into the TiO_2 for forming the ternary Cr@TiO_2/MWCNTs based NC.

Fig. 8 (b and c) shows the high resolution XPS spectra of Ti2p for TiO_2/MWCNTs and representative $Cr_{0.010}@Ti_{0.990}C$ NC respectively. After the insertion of Cr(III) ions into the TiO_2/MWCNTs NC, it shows the slight positive shifting of the Ti2p value with binding energy difference (Ti $2p_{3/2}$ and Ti $2p_{1/2}$) from 5.70 to 5.78 eV. These evidences confirms the formation of Ti-O-Cr structure in the NC after the insertion of Cr(III) indicates the substitution of Ti(IV) by Cr(III) ions into the TiO_2 host lattice of the NC (Peng et al., 2012). High resolution O 1s spectrum of $Cr_{0.010}@Ti_{0.990}C$ (Fig. 8d) shows three deconvoluted peaks. The main peak appeared at 530.4 eV attributed to the lattice oxygen (Ti-O) in anatase TiO_2, and other two peaks are located at 531.85 and 536.25 eV are assigned to the surface hydroxyl oxygen atom (Ti-OH) and carbonated oxygen atom (−COOH) respectively (V. Koli et al., 2017). However the observed binding energy of the main peak, slightly higher to that of O 1s of anatase TiO_2 (529.3 eV) which was mainly due to the variations in the electro-negativities of two metal elements viz. Ti and Cr bind with O atoms (Duan et al., 2012). Fig. 8(e) shows the high resolution C 1s spectrum of $Cr_{0.010}@Ti_{0.990}C$ NC, it shows the four deconvoluted peaks mainly 283.8, 285.52, 287.08, and 289.46 eV corresponding to the elemental carbon containing functional moieties from MWCNTs incorporated into the TiO_2 viz. O-Ti-C, C-C, C-O, and Ti-O-C respectively (V.B. Koli et al., 2017). Two peaks identified in the high resolution core level XPS spectrum of Cr 2p having binding energies of 576.14 and 585.92 eV attributed to the Cr $2p_{3/2}$ and $2p_{1/2}$ [Fig. 8(f)] (Peng et al., 2012). The existence of these peaks in the $Cr_{0.010}@Ti_{0.990}C$ NC indicates the insertion of Cr(III) ions into the TiO_2 host lattice of the TiO_2/MWCNTs NC.

Time resolved-photoluminescence (TRPL) spectroscopy gives the interfacial charge transfer process for knowing the electron-hole recombination rate of the desired NCs (Xia et al., 2017). Fig. 9 shows the TRPL spectra of TiO_2/MWCNTs and representative $Cr_{0.010}@Ti_{0.990}C$ and $Cr_{0.030}@Ti_{0.970}C$ NCs. The various fitted decay parameters obtained from the TRPL spectra viz. goodness of fit (χ^2), excited-state lifetime (τ_1, τ_2), and average excitons lifetime ($\langle\tau_a\rangle$) are summarised in Table 2.

The obtained decay parameters of the NCs (Table 2) from Fig. 9, it is seen that, the average life of the electrons in the excited state increases after the insertion of Cr(III) doping (τ_a = 38.97 ps for $Cr_{0.010}@Ti_{0.990}C$), but higher content of the doping impurities decreases all the decay parameters with average life time (τ_a = 10.45 ps for $Cr_{0.030}@Ti_{0.970}C$) indicates the higher content of Cr(III) doping hampers the interfacial charge transportation process of the NCs. Also, with increase in dopant concentration, the density of states of Cr^{3+} ions becomes more negative and which may lower than that of the energy level of FTO (−4.9 eV). This results confirms the improper electron transfer mechanism in higher content of Cr^{3+} ions doped materials.

Electrochemical impedance spectroscopic (EIS) technique has been widely utilized for knowing the kinetics of the interfacial charge transfer process occurring in the desired materials (Zhang et al., 2012). Fig. 10 shows the Nyquist plot of the EIS spectra obtained from the representative TiO_2/MWCNTs and $Cr_{0.010}@Ti_{0.990}C$ NCs measured in the frequency range from 0.1 Hz to 1.2 MHz and the fitted results such as ohmic resistance (R_o) and charge transfer resistance (R_{ct}) are also included in Table 2. It is seen that, decreases the charge transfer resistance (R_{ct}) from 88.65 Ω ($Cr_{0.000}@Ti_{1.000}C$) to 47.45 Ω ($Cr_{0.010}@Ti_{0.990}C$) after the insertion of Cr(III) doping impurities into the TiO_2 host lattice of the TiO_2/MWCNTs NCs. Because, the concentration of doping impurities acts as a charge trapping sites bellow the conduction band which retards the possibility of electron-hole recombination of the host material and hence which is suitable for better separation of charge carriers from LUMO of TiO_2 to FTO (Scheme 1).

4. Dye adsorption properties of NCs:

Quantitative measurement of the N719 dye loaded on the surface of NCs thin films (area = 1.0 cm^2) was calculated through absorption maxima of the N719 dye desorbed into the 10 mL aqueous 1 mM KOH solution and presented in Table 3.

Fig. 11 shows the UV–Visible absorption spectra of N719 dye detached from TiO_2/MWCNTs ($Cr_{0.000}@Ti_{1.000}C$) and representative $Cr_{0.010}@Ti_{0.990}C$ and $Cr_{0.030}@Ti_{0.970}C$ NCs thin film. It is seen that, as the Cr(III) content increases in TiO_2/MWCNTs NC, it also increases the adsorption capability of the N719 dye. It was may be due to the smaller crystallite size of the NCs after the insertion Cr(III) into the TiO_2 lattice, offers more dye adsorption on the surface of the NCs thin films. After the loading of N719 dye on the surface of the TiO_2/MWCNTs and Cr@TiO_2/MWCNTs NCs thin films and irradiated under light and the plausible charge transfer mechanism of the sensitized NCs are illustrated in the scheme 1.

Fig. 12 shows the photocurrent-density voltage (*I-V*) characteristics curves of the sandwiched DSSCs of bare TiO_2 (T), TiO_2/MWCNTs and Cr@TiO_2/MWCNTs NCs with varying the insertion of Cr(III) content into the TiO_2 host lattice of the TiO_2/MWCNTs NCs. The resulting various photovoltaic performance cell parameters derived from the *I-V*

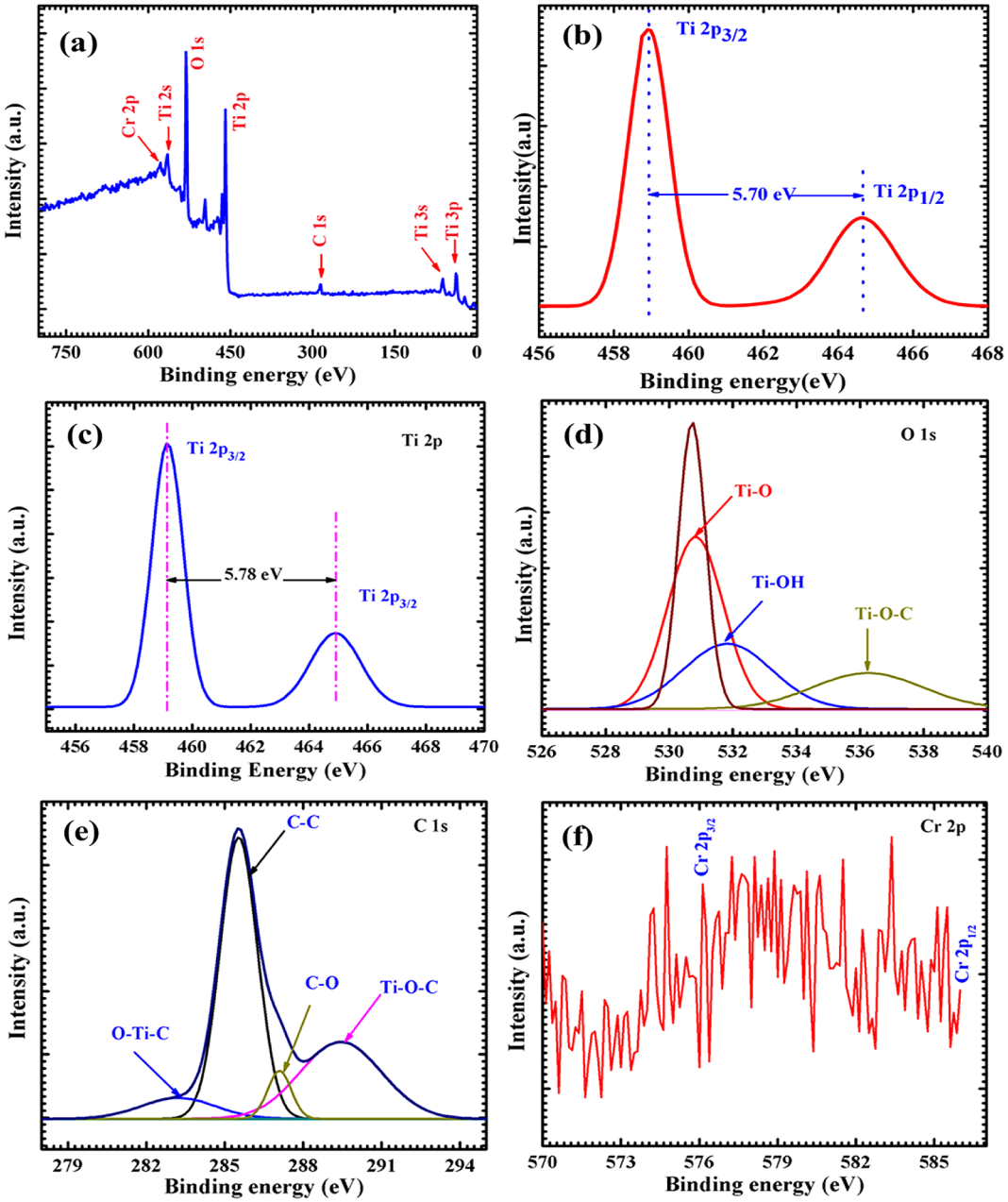

Fig. 8. (a) XPS survey spectrum of $Cr_{0.010}@Ti_{0.990}C$ NC, high resolution core level XPS spectrum of (b) Ti2p for TiO_2/MWCNTs (c) Ti2p, (d) O1s, (e) C1s, and (f) Cr2p for $Cr_{0.010}@Ti_{0.990}C$ NC thin film.

curves viz. *Jsc*, *Voc*, *FF* and η with optical energy band gap (*Eg*) and amount of dye adsorbed on the NCs thin film surface are listed in Table 3.

In the previous paper already reported, the incorporation of MWCNTs into the TiO_2 enhanced almost all the photovoltaic cell parameters of the DSSCs due to the synergistic effect of MWCNTs with TiO_2 NPs. Because, it provides higher surface area to the TiO_2 NPs for uniform anchoring purpose and hence it was betterment for higher dye loading on the surface of TiO_2 NPs of the NCs thin films. Also, it induced the enhancement of the electron transport rate of the TiO_2 host lattice for better charge transportation in the DSSCs which leads to enhance the *Jsc* value. Overall results suggested the MWCNTs must play a significant role for enhancing the conductivity of the TiO_2 host lattice for better charge separation in the DSSCs (Delekar et al., 2018). In the present investigation, the insertion of Cr(III) content into the TiO_2 host lattice of the TiO_2/MWCNTs NCs and their synergisticity on the photovoltaic performance is highlighted.

It is seen that, the boosting of the *Jsc* value was observed after the little insertion of Cr(III) into the TiO_2 host lattice of the TiO_2/MWCNTs NCs [Fig. S5(a), *SI*] from 16.88 (TiO_2/MWCNTs) to 18.33 mA/cm^2 ($Cr_{0.005}@Ti_{0.995}C$) and reached the highest *Jsc* value up to 20.38 mA/cm^2 for optimized ($Cr_{0.010}@Ti_{0.990}C$) NC, which is 21% higher *Jsc* value to that of TiO_2/MWCNTs based DSSCs. The enhancement of these *Jsc* values are collinear not only with the higher dye loading capability but also with lower optical energy band gap (Table 3) and coverage of the optical region [Fig. 5(a)] of the NCs after the substitution of Ti(IV) by Cr(III) into the TiO_2/MWCNTs NCs. A plot of Cr(III) content in mol.% as a function of *Voc* [Fig. S5(b), *SI*] shows the little enhancement of the *Voc* value from 670 mV (TiO_2/MWCNTs) to 700 mV ($Cr_{0.010}@Ti_{0.990}C$) after the insertion of Cr(III) into the TiO_2/MWCNTs NCs. It may be due to the decrease of the charge transfer resistance of the TiO_2/MWCNTs NCs with substitution of Ti(IV) by Cr(III) into the NCs (Fig. 10). It may

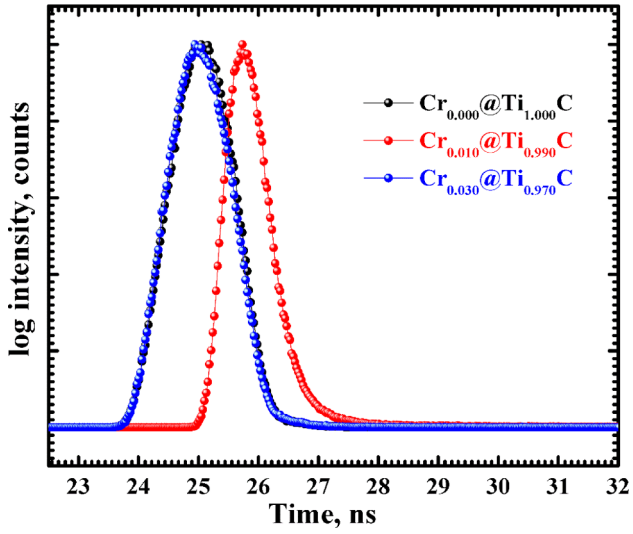

Fig. 9. Time-resolved photoluminescence (TRPL) spectra of TiO_2/MWCNTs and representative $Cr_{0.010}@Ti_{0.990}C$ and $Cr_{0.030}@Ti_{0.970}C$ NCs at an excited wavelength (475 nm).

Table 2
Time-resolved photoluminescence (TRPL) spectroscopic decay parameters such as goodness of fit (χ^2), excited-state lifetime (τ_1, τ_2), average excitons lifetime ($\langle\tau_a\rangle$) and electrochemical impedance spectroscopic (EIS) parameters viz. ohmic resistance (R_o), and charge transfer resistance (R_{ct}) of the TiO_2/MWCNTs and representative $Cr_{0.010}@Ti_{0.990}$ $Cr_{0.030}@Ti_{0.970}$ NCs.

Sample	χ^2	τ_1 (ps)	τ_2 (ps)	$\langle\tau_a\rangle$ (ps)	R_o (Ω)	R_{ct} (Ω)
$Cr_{0.000}@Ti_{1.000}C$	1.27	14.77	14.84	14.81	7.42	88.65
$Cr_{0.010}@Ti_{0.990}C$	1.55	37.88	41.27	38.97	6.47	47.45
$Cr_{0.030}@Ti_{0.970}C$	1.07	5.44	14.43	10.45	–	–

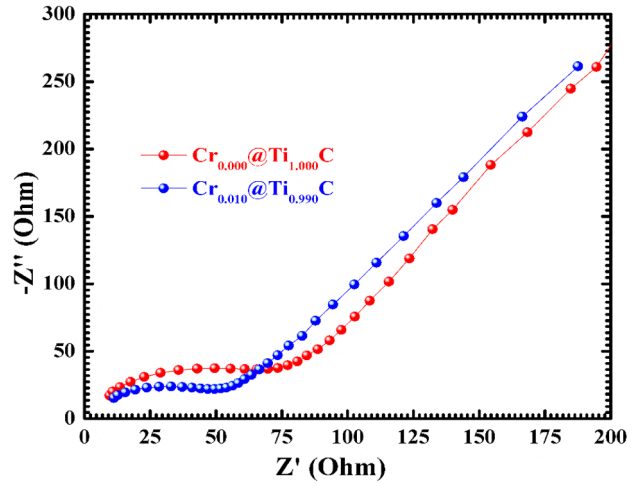

Fig. 10. Nyquist plot of the representative $Cr_{0.000}@Ti_{1.000}C$ and $Cr_{0.010}@Ti_{0.990}C$ NCs in the dark at 0.1 Hz to 1.2 MHz frequency.

be due to the doping content into the TiO_2 host lattice enhances the concentration of doping impurities and which could acts as charge trapping sites (scheme 1) and improves the charge transportation rate in the DSSCs (Duan et al., 2012). The insertion of doping impurities in TiO_2/MWCNTs shows no significant effects on the *FF* value, which is seen in the supporting information [Fig. S5(c), *SI*]. From the photovoltaic measurements, a plot of Cr(III) content in mol.% vs power conversion efficiency (PCE) shows [Fig. S5(d), *SI*] the PCE (η) enhances up to 10% (η = 6.79%) for $Cr_{0.005}@Ti_{0.995}C$ NC and reached up to 25% (η = 7.69%) higher for optimized $Cr_{0.010}@Ti_{0.990}C$ NC to that of TiO_2/MWCNTs NCs based DSSCs (η = 6.18%). These enhancement of the PCE value after the substitution of Ti(IV) by Cr(III), it may be due to the lower optical energy band gap and higher average life-time of the electrons in the excited state (Fig. 9) enhances the electron transportation rate from LUMO of the NCs to FTO (scheme 1) and finally to the counter electrode. Overall results, it is seen that, the significant enhancement of the almost all the photovoltaic performance cell parameters after the little insertion of doping impurities ($Cr_{0.010}@Ti_{0.990}C$) into the TiO_2 host lattice of the TiO_2/MWCNTs NCs. However, it is seen that, the higher content of doping impurities ($Cr_{0.030}@Ti_{0.970}C$), contrariwise all the photovoltaic performance cell parameters as *Jsc* = 20.387–17.265 mA/cm^2, *Voc* = 700–590 mV, *FF* = 53.91–46.31% and *η* = 7.69–4.71 respectively. It could be attributed to the higher concentration of doping impurities may be acts as a charge trapping sites for promoting the electron-hole recombination also and hence leading to decrease all the photovoltaic performance cell parameters (Burschka et al., 2011).

To evaluate the performance of the representative TiO_2/MWCNTs and $Cr_{0.010}@Ti_{0.990}C$ NCs as a photoelectrode for photovoltaic application by measuring the incident photon-to-current conversion efficiency (IPCE) of the sandwiched DSSCs with respect to wavelength of incident light. Fig. 13 shows the IPCE response of TiO_2/MWCNTs compared with the representative $Cr_{0.010}@Ti_{0.990}C$ NCs based DSSCs.

It is seen that, $Cr_{0.010}@Ti_{0.990}C$ NC have higher IPCE response to that of TiO_2/MWCNTs NC based DSSCs in all the entire wavelength region, which is also in good agreement with the highest *Jsc* value from *I-V* measurements after the insertion of Cr(III). Both the NCs shows the generation of photocurrent in the wavelength region between 300 and 650 nm and maximum photocurrent response appeared in the two distinct regions viz. 300–400 nm and 475–650 nm respectively. The IPCE response enhanced from ~58.2% to ~70.7% in the visible wavelength region at 475–800 nm with additional coverage of the optical region after the insertion doping into the host of the TiO_2/MWCNTs NCs. The observed results suggesting that doping impurities enhances the electron transport in the TiO_2/MWCNTs NCs thin film with suppression of back-electron transfer towards HOMO of sensitizer and hence its impact on the boosting of the overall power conversion efficiency after the substitution of Ti(IV) ions by Cr(III) ions.

5. Conclusions

The synergistic effect of Cr(III) doping with hybrid TiO_2/MWCNTs NCs enhances the optoelectronic behavior and exhibiting the highest power conversion efficiency value of η = 7.69% which appose to an conversion efficiency of TiO_2/MWCNTs (η = 6.18%) and bare TiO_2 (η = 1.52%) based DSSCs measured under one sun irradiation (100 mW/cm^2). Initially, a facile, single step *in-situ sol-gel* approach have been developed for the preparation of hybrid ternary Cr@TiO_2/MWCNTs NCs. FT-IR and XPS study reveals that the substitution of Ti (IV) ions by Cr(III) ions into the TiO_2 host lattice of the TiO_2/MWCNTs NCs. The insertion of Cr(III) in TiO_2/MWCNTs varied the structural parameters and position of elements of the anatase TiO_2 which was confirmed by Rietveld analysis. Also, the interfacial charge transfer behaviors of the NCs with the content of dopant were confirmed through TRPL and EIS measurements. Afterthat, binder-free thin films of the NCs were fabricated through doctor-blade technique for the designing of sandwiched DSSCs and finally sandwiched DSSCs were measured under AM 1.5 solar simulator.

Author contributions

The final version of the manuscript approved by all complainants.

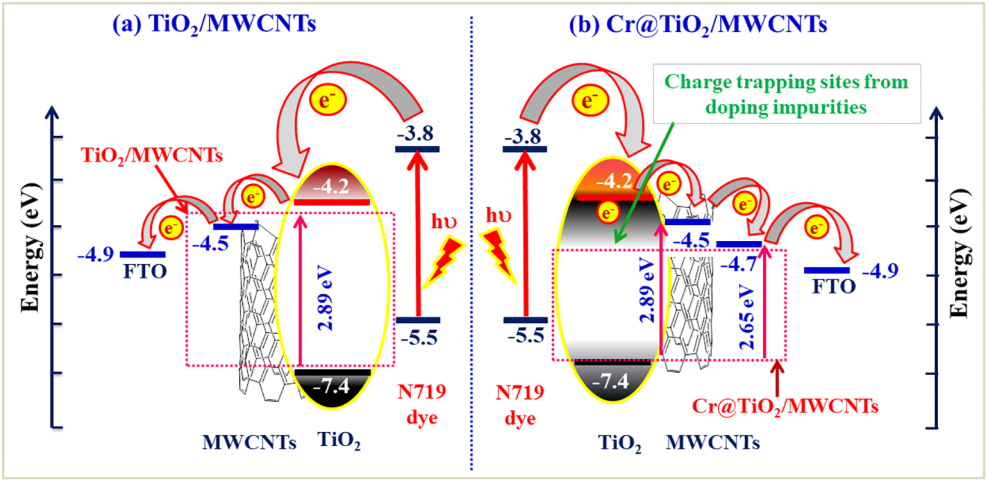

Scheme 1. Schematic representation of the plausible charge transfer mechanism of the (a) TiO_2/MWCNTs and (b) Cr@TiO_2/MWCNTs NCs sensitized with N719 dye under irradiation of light.

Table 3
Energy band gap (eV), amount of dye adsorbed on the surface of NCs thin film with photovoltaic cell parameters of the TiO_2 (T), TiO_2/MWCNTs and Cr@TiO_2/MWCNTs NCs based DSSCs with varying the content of Cr(III) in mol.%.

Samples	Cr(III) in mol.%	*Eg* (eV)	Amount of dye adsorbed (10^{-8} mol./cm^2)	Solar Cell Parameters			
				Jsc (mA/cm^2)	*Voc* (mV)	*FF* (%)	η (%)
TiO_2(T)	0.00	3.19	–	07.221	450	46.91	1.52
$Cr_{0.000}@Ti_{1.000}C$	0.00	2.89	3.26	16.887	670	54.63	6.18
$Cr_{0.005}@Ti_{0.995}C$	0.50	2.81	–	18.335	680	54.53	6.79
$Cr_{0.010}@Ti_{0.990}C$	**1.00**	**2.65**	**4.58**	**20.387**	**700**	**53.91**	**7.69**
$Cr_{0.030}@Ti_{0.970}C$	3.00	2.54	4.12	17.265	590	46.31	4.71

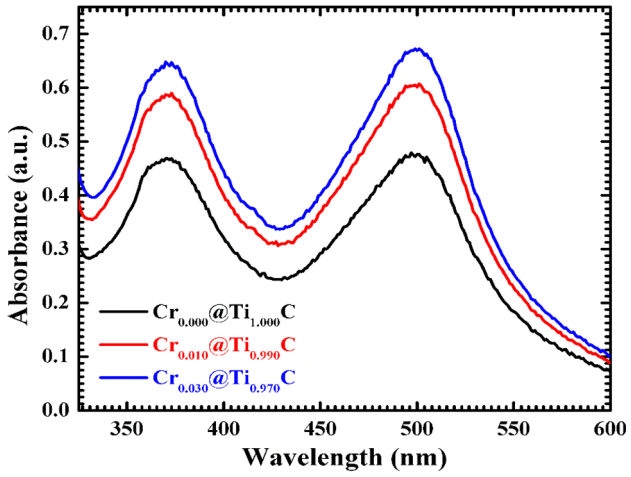

Fig. 11. UV–Visible absorption spectra of N719 dye detached from TiO_2/MWCNTs and representative $Cr_{0.010}@Ti_{0.990}C$ and $Cr_{0.030}@Ti_{0.970}C$ NCs thin films (area = 1.0 cm^2) into 10 mL aqueous 1 mM KOH solution.

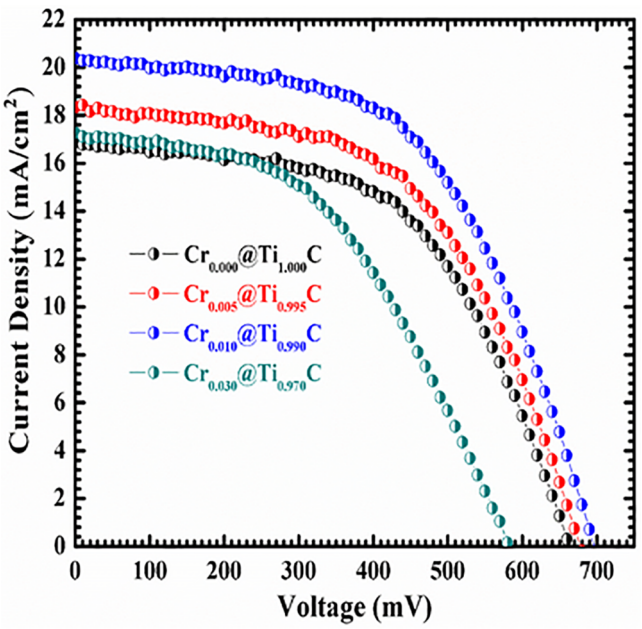

Fig. 12. Photocurrent-density voltage (*I-V*) characteristics curves of the bare TiO_2 (T), TiO_2/MWCNTs and Cr@TiO_2/MWCNTs NCs with varying the content of Cr(III) (0.5–3.0 mol.%).

Declaration of Competing Interest

There are no conflicts to declare.

Acknowledgments

Author, AGD thanks to University Grant Commission, New Delhi, India, for the financial support under the scheme of Rajiv Gandhi National Research Fellowship (UGC No. F./2014-15/RGNF-2014-15D-SC-MAH- 61438 dated, February 2015. And author SDD thanks to Shivaji University, Kolhapur for financial support under Research Strengthening Scheme (SU/C&U.D. Section/85/1383 dated, 28th March, 2019).

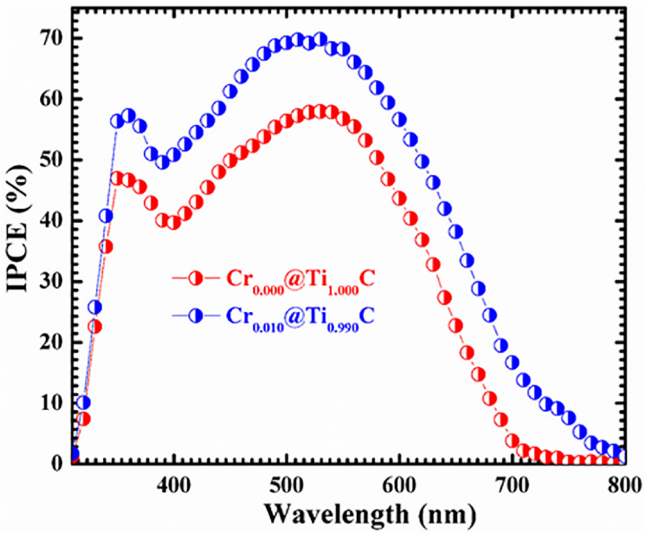

Fig. 13. IPCE spectra of TiO_2/MWCNTs ($Cr_{0.000}@Ti_{1.000}C$) compared with representative $Cr_{0.010}@Ti_{0.990}C$ NC based DSSCs.

Appendix A. Supplementary material

XRD profile of bare MWCNTs, Rietveld refinement patterns of Cr@TiO_2/MWCNTs (0.0–3.0 mol.%), Raman spectrum of bare TiO_2 NPs, UV–Visible DRS with Tauc plot of bare TiO_2 NPs and TiO_2/MWCNTs NC, plot of different photovoltaic parameters vs. Cr(III) in mol.%. This material is available free of charge via the internet at http://www.elsevier.com. Supplementary data to this article can be found online at https://doi.org/10.1016/j.solener.2020.03.001.

References

Bai, Y., Mora-Sero, I., De Angelis, F., Bisquert, J., Wang, P., 2014. Titanium dioxide nanomaterials for photovoltaic applications. Chem. Rev. 114 (19), 10095–10130.

Burschka, J., Dualeh, A., Kessler, F., Baranoff, E., Cevey-Ha, N.-L., Yi, C., Nazeeruddin, M.K., Grätzel, M., 2011. Tris(2-(1H-pyrazol-1-yl)pyridine)cobalt(III) as p-type dopant for organic semiconductors and its application in highly efficient solid-state dye-sensitized solar cells. J. Am. Chem. Soc. 133 (45), 18042–18045.

Cao, J., Zhang, Y., Liu, L., Ye, J., 2013. A p-type Cr-doped TiO_2 photo-electrode for photo-reduction. Chem. Commun. 49 (33), 3440–3442.

Chen, D., Wang, Q., Wang, R., Shen, G., 2015. Ternary oxide nanostructured materials for supercapacitors: a review. J. Mat. Chem. A 3 (19), 10158–10173.

De Angelis, F., Fantacci, S., Mosconi, E., Nazeeruddin, M.K., Grätzel, M., 2011. Absorption spectra and excited state energy levels of the N719 dye on TiO_2 in dye-sensitized solar cell models. J. Phy. Chem. C 115 (17), 8825–8831.

Delekar, S.D., Dhodamani, A.G., More, K.V., Dongale, T.D., Kamat, R.K., Acquah, S.F.A., Dalal, N.S., Panda, D.K., 2018. Structural and optical properties of nanocrystalline TiO_2 with multiwalled carbon nanotubes and its photovoltaic studies using Ru(II) sensitizers. ACS Omega 3 (3), 2743–2756.

Deng, Y., Tang, L., Zeng, G., Feng, C., Dong, H., Wang, J., Feng, H., Liu, Y., Zhou, Y., Pang, Y., 2017. Plasmonic resonance excited dual Z-scheme $BiVO_4$/Ag/Cu_2O nanocomposite: synthesis and mechanism for enhanced photocatalytic performance in recalcitrant antibiotic degradation. Environ. Sci. Nano 4 (7), 1494–1511.

Dette, C., Pérez-Osorio, M.A., Kley, C.S., Punke, P., Patrick, C.E., Jacobson, P., Giustino, F., Jung, S.J., Kern, K., 2014. TiO_2 anatase with a bandgap in the visible region. Nano Lett. 14 (11), 6533–6538.

Dhodamani, A.G., More, K.V., Koli, V.B., Shelke, A.R., Deshpande, N.G., Panda, D.K., Delekar, S.D., 2019. Compositional dependent physicochemical and photovoltaic properties of the $(TiO_2)_{1-x}(RGO_x$ nanocomposites for sensitized solar cells using Ru (II) dyes. ChemistrySelect 4 (3), 1055–1068.

Dholam, R., Patel, N., Adami, M., Miotello, A., 2009. Hydrogen production by photocatalytic water-splitting using Cr-or Fe-doped TiO_2 composite thin films photocatalyst. Int. J. Hydrogen Energ. 34 (13), 5337–5346.

Duan, Y., Fu, N., Liu, Q., Fang, Y., Zhou, X., Zhang, J., Lin, Y., 2012. Sn-doped TiO_2 photoanode for dye-sensitized solar cells. J. Phy. Chem. C 116 (16), 8888–8893.

Hu, Y., Liu, X., Tian, L., Zhao, T., Wang, H., Liang, X., Zhou, F., Zhu, P., Li, G., Sun, R., Wong, C.-P., 2018. Multidimensional ternary hybrids with synergistically enhanced electrical performance for conductive nanocomposites and prosthetic electronic skin. ACS Appl. Mater. Interfaces 10 (44), 38493–38505.

Hwang, D.W., Kim, H.G., Lee, J.S., Kim, J., Li, W., Oh, S.H., 2005. Photocatalytic hydrogen production from water over M-doped $La_2Ti_2O_7$ (M = Cr, Fe) under visible light irradiation (λ > 420 nm). J. Phy. Chem. B 109 (6), 2093–2102.

Ikeda, T., Nomoto, T., Eda, K., Mizutani, Y., Kato, H., Kudo, A., Onishi, H., 2008. Photoinduced dynamics of TiO_2 doped with Cr and Sb. J. Phy. Chem. C 112 (4), 1167–1173.

Inturi, S.N.R., Boningari, T., Suidan, M., Smirniotis, P.G., 2014a. Flame aerosol synthesized Cr incorporated TiO_2 for visible light photodegradation of gas phase acetonitrile. J. Phy. Chem. C 118 (1), 231–242.

Inturi, S.N.R., Boningari, T., Suidan, M., Smirniotis, P.G., 2014b. Visible-light-induced photodegradation of gas phase acetonitrile using aerosol-made transition metal (V, Cr, Fe Co, Mn, Mo, Ni, Cu, Y, Ce, and Zr) doped TiO2. App. Cat. B: Env. 144, 333–342.

Kakiage, K., Aoyama, Y., Yano, T., Oya, K., Fujisawa, J.-I., Hanaya, M., 2015. Highly-efficient dye-sensitized solar cells with collaborative sensitization by silyl-anchor and carboxy-anchor dyes. Chem. Commun. 51 (88), 15894–15897.

Koli, V., Dhodamani, A., More, K., Acquah, S.F., Panda, D.K., Pawar, S., Delekar, S., 2017a. A simple strategy for the anchoring of anatase titania on multi-walled carbon nanotubes for solar energy harvesting. Sol. Energy 149, 188–194.

Koli, V.B., Dhodamani, A.G., Delekar, S.D., Pawar, S.H., 2017b. In situ sol-gel synthesis of anatase TiO_2-MWCNTs nanocomposites and their photocatalytic applications. J. Photochem. Photobiol. 333, 40–48.

Kumar, A., Rout, L., Achary, L.S.K., Mohanty, A., Dhaka, R.S., Dash, P., 2016. An investigation into the solar light-driven enhanced photocatalytic properties of a graphene oxide–SnO_2–TiO_2 ternary nanocomposite. RSC Adv. 6 (38), 32074–32088.

Lee, J.S., You, K.H., Park, C.B., 2012. Highly photoactive, low bandgap TiO_2 nanoparticles wrapped by graphene. Adv. Mater. 24 (8), 1084–1088.

Liu, C., Yang, D., Jiao, Y., Tian, Y., Wang, Y., Jiang, Z., 2013. Biomimetic synthesis of TiO_2–SiO_2–Ag nanocomposites with enhanced visible-light photocatalytic activity. ACS Appl. Mater. Interfaces 5 (9), 3824–3832.

Malik, R., Tomer, V.K., Joshi, N., Dankwort, T., Lin, L., Kienle, L., 2018. Au–TiO2-loaded cubic g-C_3N_4 nanohybrids for photocatalytic and volatile organic amine sensing applications. ACS Appl. Mater. Interfaces 10 (40), 34087–34097.

Mamba, G., Mamo, M.A., Mbianda, X.Y., Mishra, A.K., 2014. Nd, N, S-TiO_2 decorated on reduced graphene oxide for a visible light active photocatalyst for dye degradation: comparison to its MWCNT/Nd, N, S-TiO_2 analogue. Ind. Eng. Chem. Res. 53 (37), 14329–14338.

Mao, B., Chuang, C.-H., Wang, J., Burda, C., 2011. Synthesis and photophysical properties of ternary I-III–VI $AgInS_2$ nanocrystals: intrinsic versus surface states. J. Phy. Chem. C 115 (18), 8945–8954.

Mao, G., Xu, M., Yao, S., Zhou, B., Liu, Q., 2018. Direct growth of Cr-doped TiO_2 nanosheet arrays on stainless steel substrates with visible-light photoelectrochemical properties. New J. Chem. 42 (2), 1309–1315.

Mathew, S., Yella, A., Gao, P., Humphry-Baker, R., Curchod, B.F., Ashari-Astani, N., Tavernelli, I., Rothlisberger, U., Nazeeruddin, M.K., Grätzel, M., 2014. Dye-sensitized solar cells with 13% efficiency achieved through the molecular engineering of porphyrin sensitizers. Nat. Chem. 6 (3), 242.

Miao, R., He, J., Sahoo, S., Luo, Z., Zhong, W., Chen, S.-Y., Guild, C., Jafari, T., Dutta, B., Cetegen, S.A., Wang, M., Alpay, S.P., Suib, S.L., 2017. Reduced graphene oxide supported nickel–manganese–cobalt spinel ternary oxide nanocomposites and their chemically converted sulfide nanocomposites as efficient electrocatalysts for alkaline water splitting. ACS Catal. 7 (1), 819–832.

Mondal, S., Aepuru, R., Dana, J., Ghorai, N., Ghosh, H.N., 2018. Bi-exciton dissociation dynamics in nano-hybrid Au-$CuInS_2$ nanocrystals. J. Phy. Chem. C.

Oregan, B., Grätzel, M., 1991. A low-cost, high-efficiency solar cell based on dye-sensitized colloidal TiO2 films. Nature 353 (6346), 737.

Ou, J.Z., Rani, R.A., Ham, M.-H., Field, M.R., Zhang, Y., Zheng, H., Reece, P., Zhuiykov, S., Sriram, S., Bhaskaran, M., 2012. Elevated temperature anodized Nb2O5: a photoanode material with exceptionally large photoconversion efficiencies. ACS Nano 6 (5), 4045–4053.

Pan, Z., Zhang, H., Cheng, K., Hou, Y., Hua, J., Zhong, X., 2012. Highly efficient inverted type-I CdS/CdSe core/shell structure QD-sensitized solar cells. ACS Nano 6 (5), 3982–3991.

Peng, Y.-H., Huang, G.-F., Huang, W.-Q., 2012. Visible-light absorption and photocatalytic activity of Cr-doped TiO_2 nanocrystal films. Adv. Powder Technol. 23 (1), 8–12.

Rakhi, R.B., Chen, W., Cha, D., Alshareef, H.N., 2012. Nanostructured ternary electrodes for energy-storage applications. Adv. Energy Mater. 2 (3), 381–389.

Regulacio, M.D., Wang, Y., Seh, Z.W., Han, M.-Y., 2018. Tailoring porosity in copper-based multinary sulfide nanostructures for energy, biomedical, catalytic, and sensing applications. ACS Appl. Nano Mater. 1 (7), 3042–3062.

Sakai, N., Miyasaka, T., Murakami, T.N., 2013. Efficiency enhancement of ZnO-based dye-sensitized solar cells by low-temperature $TiCl_4$ treatment and dye optimization. J. Phy. Chem. C 117 (21), 10949–10956.

Santra, P.K., Kamat, P.V., 2013. Tandem-layered quantum dot solar cells: tuning the photovoltaic response with luminescent ternary cadmium chalcogenides. J. Am. Chem. Soc. 135 (2), 877–885.

Shevale, V.B., Dhodamani, A.G., Koli, V.B., Barkul, R.P., Jadhav, J.P., Delekar, S.D., 2017. Efficient degradation of Azorubin S colourant in the commercial jam-jelly food samples using TiO_2-$CoFe_2O_4$ nanocomposites in visible light. Mater. Res. Bull. 89, 79–88.

Shwetharani, R., Sakar, M., Fernando, C.A.N., Binas, V., Balakrishna, R.G., 2019. Recent advances and strategies to tailor the energy levels, active sites and electron mobility in titania and its doped/composite analogues for hydrogen evolution in sunlight. Catal. Sci. Technol.

Snaith, H.J., Ducati, C., 2010. SnO_2-based dye-sensitized hybrid solar cells exhibiting near unity absorbed photon-to-electron conversion efficiency. Nano Lett. 10 (4), 1259–1265.

Tang, R., Yin, L., 2015. Enhanced photovoltaic performance of dye-sensitized solar cells based on Sr-doped TiO_2/$SrTiO_3$ nanorod array heterostructures. J. Mater. Chem. A 3

(33), 17417–17425.
Tian, F., Zhang, Y., Zhang, J., Pan, C., 2012. Raman spectroscopy: a new approach to measure the percentage of anatase TiO_2 exposed (001) facets. J. Phy. Chem. C 116 (13), 7515–7519.
Wang, C., Shi, H., Li, Y., 2012. Synthesis and characterization of natural zeolite supported Cr-doped TiO_2 photocatalysts. Appl. Surf. Sci. 258 (10), 4328–4333.
Wang, Y., Bai, L., Wang, Y., Qin, D., Shan, D., Lu, X., 2018. Ternary nanocomposites of Au/CuS/TiO_2 for an ultrasensitive photoelectrochemical non-enzymatic glucose sensor. Analyst 143 (7), 1699–1704.
Xia, P., Zhu, B., Yu, J., Cao, S., Jaroniec, M., 2017. Ultra-thin nanosheet assemblies of graphitic carbon nitride for enhanced photocatalytic CO_2 reduction. J. Mater. Chem. A 5 (7), 3230–3238.
Xie, Y., Huang, N., You, S., Liu, Y., Sebo, B., Liang, L., Fang, X., Liu, W., Guo, S., Zhao, X.-Z., 2013. Improved performance of dye-sensitized solar cells by trace amount Cr-doped TiO_2 photoelectrodes. J. Power Sources 224, 168–173.
Yan, H., Tian, X., Pang, Y., Feng, B., Duan, K., Zhou, Z., Weng, J., Wang, J., 2016. Heterostructured gC_3N_4/Ag/TiO_2 nanocomposites for enhancing the photoelectric conversion efficiency of spiro-OMeTAD-based solid-state dye-sensitized solar cells. RSC Adv. 6 (104), 102444–102452.
Yue, Y., Juarez-Robles, D., Chen, Y., Ma, L., Kuo, W.C., Mukherjee, P., Liang, H., 2017. Hierarchical Structured Cu/Ni/TiO_2 Nanocomposites as Electrodes for Lithium-Ion Batteries. ACS Appl. Mater. Interfaces 9 (34), 28695–28703.
Yun, S., Qin, Y., Uhl, A.R., Vlachopoulos, N., Yin, M., Li, D., Han, X., Hagfeldt, A., 2018. New-generation integrated devices based on dye-sensitized and perovskite solar cells. Energy Environ. Sci. 11 (3), 476–526.
Zhang, H., Cheng, K., Hou, Y., Fang, Z., Pan, Z., Wu, W., Hua, J., Zhong, X., 2012. Efficient CdSe quantum dot-sensitized solar cells prepared by a postsynthesis assembly approach. Chem. Commun. 48 (91), 11235–11237.
Zhu, H., Tao, J., Dong, X., 2010. Preparation and photoelectrochemical activity of Cr-doped TiO_2 nanorods with nanocavities. J. Phy. Chem. C 114 (7), 2873–2879.
Zhu, J., Deng, Z., Chen, F., Zhang, J., Chen, H., Anpo, M., Huang, J., Zhang, L., 2006. Hydrothermal doping method for preparation of Cr^{3+}-TiO_2 photocatalysts with concentration gradient distribution of Cr^{3+}. Appl. Catal., B 62 (3–4), 329–335.